Title

Shape dependence of wind pressure peak factor statistics in hyperbolic paraboloid roofs

Authors

Rizzo, Fabio
Barbato, Michele
Sepe, Vincenzo

Publication Date

2021-12-01

DOI

10.1016/j.jobe.2021.103203

Peer reviewed

SHAPE DEPENDENCE OF WIND PRESSURE PEAK FACTOR STATISTICS IN HYPERBOLIC PARABOLOID ROOFS

Fabio Rizzo[1*], Michele Barbato[2], Vincenzo Sepe[3]

[1] University "G. D'Annunzio" of Chieti-Pescara, Viale Pindaro 42, 65127 Pescara, Italy, fabio.rizzo@unich.it (*corresponding author)
[2] University of California - Davis, 3149 Ghausi Hall, One Shields Avenue, Davis, CA 95616, USA, mbarbato@ucdavis.edu
[3] University "G. D'Annunzio" of Chieti-Pescara, Viale Pindaro 42, 65127 Pescara, Italy, v.sepe@unich.it

Abstract

The complex shape dependence of wind pressure's peak factors (PFs) makes it difficult to predict their values for all geometries by using analytical models. Thus, experimental studies are necessary to validate available or new analytical models for each specific shape and geometry. Very little information is available in the literature for the hyperbolic paraboloid geometry, which is frequently used for cable net and membrane roofs that are particularly appropriate for covering large spans. This paper focuses on wind pressure's PFs for this specific geometry. It presents a statistical analysis of experimental data taken from wind tunnel experiments on eight different geometries, obtained through the combinations of squared and rectangular plan shapes, high and low models, and two different curvatures of the roof parabolas. Roof zones for which a non-Gaussian behavior is predominant are identified. A comparison is made between PF statistics obtained experimentally and those estimated by the Davenport, modified Hermite, and Translated Peak Process (TPP) models, in terms of means and standard deviation errors estimated over the entire roofs. It is concluded that the modified Hermite and the TPP models provide the best estimates of the PF means and standard deviations, respectively.

Keywords:

Pressure coefficients; peak factors; random processes; hyperbolic paraboloid roofs; aerodynamics.

1. INTRODUCTION

Hyperbolic paraboloid shapes are often employed in tensile roof structures with very large spans (Chilton 2010; Huntington 2004, 2013; Rizzo and Zazzini 2016, 2017). The structural reliability of cables structures and in particular of hyperbolic paraboloid cable nets under wind actions crucially depends on their aerodynamic and aeroelastic response, the knowledge of which is limited (Colliers et al. 2016, 2019, 2020; Elashkar and Novak 1983; Foster and Mollaert 2004; Letchford et al. 2002; Majowiecki 2004; Rizzo et al. 2011, 2018, 2020; Rizzo and Ricciardelli 2017; Rizzo 2014; Vassilopoulou and Gantes 2011, 2012). In addition, performance-based design approaches applied to wind and hurricane engineering require the accurate estimation and prediction of extreme wind action (Barbato et al. 2013; Ciampoli and Petrini 2012; Unnithan and Barbato 2016) and, thus, of wind pressure peak factors (PFs) (Kwon and Kareem 2011).

For hyperbolic paraboloid roofs (HPRs) made of cable nets, the roof stiffness depends on the roof geometry, the initial pretensioning strain of the cables, and the roof deformation induced by the applied loads. Under upward loads, as those generated by strong winds, the strain in the sagging (upward curvature) cables decreases as the cables flatten. Under large displacements, these cables can invert their curvatures and produce local/global instability (Majowiecki 2004). By contrast, the strain in hogging (downward curvature) cables increases, potentially leading to brittle failure of the cables. This local failure can then lead to the global instability of the entire roof structure (Majowiecki 2004). As a result, the structural performance of these structures is particularly sensitive to high local values of the wind pressure PFs. In addition, existing technical standards and design codes (e.g., CNR 2018) provide average and/or maximum (positive and negative) wind pressure coefficients to assess both global effects on HPR cable net structures and local effects on membrane panels. However, these pressure coefficients cannot be used to assess the local instability

and brittle failure effects that can be produced by localized large fluctuations in the wind pressure, which can be described only through appropriate statistics of the wind pressure PFs. Large differences between the PFs on edge and interior regions of HPRs have been observed (Rizzo et al. 2018), suggesting that roof areas with similar mean wind pressure coefficients can be subjected to very different peak wind pressures.

An important aspect in the calculation of the PFs and their statistics is the nature of the underlying stochastic process (i.e., Gaussian or non-Gaussian process), which determines the appropriateness and accuracy of the different numerical approaches available in the literature for different applications. In particular, if the underlying stochastic process is (at least approximately) Gaussian, the Davenport model is able to estimate accurately the PF means and standard deviations (Davenport 1964, Gurley et al. 1997). However, if the process is non-Gaussian, no exact solutions are available in the literature to predict the PF statistics. In general, Gaussian approximations yield non-conservative estimates of the PF values when applied to non-Gaussian processes (Kareem and Zhao 1994), and different approximate models have been developed to estimate the PF statistics of non-Gaussian processes (Huang et al. 2013; Kareem and Zhao 1994; Kwon and Kareem 2011; Sadek and Simiu 2002). Very few studies available in the literature investigated the PFs and their statistics for hyperbolic paraboloid roofs (HPRs) (Liu et al. 2016, 2017; Rizzo et al. 2018). Liu et al. (2016) investigated several statistics of wind pressure on a saddle-type HPR with linear edges and their dependence on different turbulence profiles. They observed that the PFs in the flow detachment roof areas present a clear non-Gaussian behavior and that moment-based Hermite estimates are accurate only for mild non-Gaussianity. Rizzo et al. (2018) investigated the non-Gaussianity of the pressure coefficient processes for a square HPR through a comparison between experimental measures and analytical estimates of PF statistics. They observed that: (1) the distribution of non-Gaussian regions strongly depend on the wind

angle, (2) the Davenport model systematically underestimates the PF mean and standard deviation in highly non-Gaussian regions, (3) moment-based Hermite models provide accurate estimates of the PF mean, and (4) the Translated-Peak-Process (TPP) model (Huang et al. 2013) seems to provide the best estimates of the PF standard deviation. Rizzo et al. (2018) also observed that the local variability of the pressure coefficient peaks is best described by a Weibull distribution, as assumed by the TPP model. Liu et al. (2017) proposed a modification of the moment-based Hermite model that uses two different distributions to describe the maxima and minima of the pressure coefficients and obtain improved estimates of the PFs for large-span saddle-type HPRs. Existing literature indicates that the local wind pressure coefficients are also highly dependent on the shape and geometry of the HPR under investigation (Rizzo et al. 2011, 2018, 2020). However, a rigorous investigation is still needed to determine the shape and geometry dependence of the PFs for this type of roofs, as well as of the accuracy and applicability to HPRs of existing approximations to estimate PF statistics.

This study investigates the Gaussianity of pressure coefficient processes and the PF statistics for HPRs as a function of wind angle of attack, shape, geometry, and location within the roofs. Experimental results obtained through wind tunnel measurements are presented for a set of square and rectangular HPR models with two different heights and two different roof curvatures, for a total of eight different HPR models. Experimental measurements and analytical estimates of PF statistics are critically compared to derive general indications on the accuracy and applicability of the different analytical models considered in this study for use with HPRs.

2. MOTIVATION, NOVELTY AND RELEVANCE

This study focuses on developing new information regarding the wind loading on HPRs, as well as on demonstrating the need to integrate the resulting new knowledge within

current technical standards and modern design codes, particularly for performance-based design applications, which require accurate probabilistic models of both global and local wind actions. In particular, accurate estimates of wind pressure PFs are essential to develop design guidelines directed to avoid local failures and local instability phenomena in flexible HPR cable structures.

This study provides two main novel contributions to engineering knowledge: (1) the documentation and detailed discussion of new experimental data on the statistics of wind pressure coefficients (i.e., skewness coefficient, excess kurtosis, and mean zero-crossing rate of pressure coefficients, as well as mean and standard deviation of peak factors) for eight different geometries of HPRs; and (2) the rigorous comparison of three well-known analytical models available in the literature in terms of their relative accuracy (expressed in terms of global error measures calculated over the entire roof) to estimate the statistics of wind pressure PFs when applied to HPRs, in order to generalize the results presented in Rizzo et al. (2018) for a single HPR geometry to different HPR shapes and geometries. To the authors' knowledge, this study is the first one to investigate such a wide range of parameters (i.e., wind angle of attack, shape, geometry, and location within the roofs) with the specific intent to reach general conclusions for wind pressure PFs of HPRs (i.e., in terms of Gaussianity or non-Gaussianity of the underlying processes, and accuracy of different analytical models in estimating the statistics of the wind pressure PFs).

Both the documentation of new experimental data and the recommendation of appropriate analytical models to estimate the wind pressure PF statistics are crucial steps toward the revision and improvement of existing design specifications presented in modern design codes, as discussed in Rizzo et al. (2018). In addition, the results reported in this study could also be directly used to analytically estimate the wind pressure PFs in performance-based design approaches of HPR structures with geometric characteristics

similar to those investigated here.

3. WIND TUNNEL TESTS MODELS AND SETUP

This study focuses on the aerodynamic behavior of HPRs, whereas the wind-structure interaction of HPRs deforming under wind actions (i.e., the aeroelastic behavior of flexible HPRs) is out of the scope of this investigation. It is noted here that the investigation of wind-structure interaction for flexible structures necessarily requires two separate but interdependent phases, i.e., investigation of the aerodynamic behavior (which is the focus of the present research), and investigation of the aeroelastic behavior. In the first phase, (local and global) pressure coefficients, which are needed for the preliminary dimensioning and design of the structure, are always estimated by using rigid models in wind tunnels (e.g., Rizzo et al. 2011, Alrawashdeh and Stathopoulos 2015, Liu et al. 2016). When designing a new structure, these two phases are intertwined components of an iterative process, in which the aeroelastic investigation informs necessary changes in the shape of the structure, which then affect its aerodynamics. However, structural deflections of well-designed HPRs under wind actions are often too small to affect the corresponding wind pressure coefficients.

Experimental PFs were measured for eight different shapes of HPRs in a wind tunnel experimental campaign. These experimental tests were carried out in the CRIACIV's open circuit boundary layer wind tunnel in Prato (Italy) (Rizzo et al. 2011, 2018, 2020), with a chamber size of 2.3 m x 1.6 m. The mean wind speed profile in the wind tunnel tests was measured before placement of the model, as shown in Rizzo and Ricciardelli (2017). The wind tunnel tests were calibrated to represent an exposure category III of EN-1991, i.e., z_0 = 0.3 m (CEN 2005). The corresponding scaled roughness length was estimated as z_0 = 0.25 cm by fitting the experimental wind velocities in the range of the heights of interest, assuming a geometric scale of 1:100. At the roof level, the turbulence intensity ranged between 11%

and 12%. The tests were performed with a mean wind speed of 16.7 m/s at a height of 10 cm, which corresponds to a mean wind speed equal to 27 m/s at 10 m of height for the 1:100 geometric scale considered. The test were performed using an acquisition frequency of 252 Hz and an acquisition time T_0 = 29.77 s, with a total of 7504 time steps for each record. This acquisition time corresponds to a duration time of approximately 1800 s at full scale. Rizzo et al. (2018) showed that this acquisition time is sufficient for the pressure coefficient's statistical moments (mean, standard deviation, skewness, and excess kurtosis) to achieve their converged constant values for the underlying stationary processes. Physical scaled models were made of wood and pressure transducers were connected to polytetrafluoroethylene tubes located inside the models. The measurement accuracy was ensured via a metrological traceability chain, with a nominal accuracy of 2.5 Pa (0.25 mm water column), corresponding to less than 4% of the lowest mean pressures measured over the roofs of the physical models. Additional uncertainties potentially associated with imperfections in the fabrication of the physical models and with the wind angles of attack were considered negligible. Because the physical models were rigid, only the aerodynamic behavior of HPRs was investigated in this study.

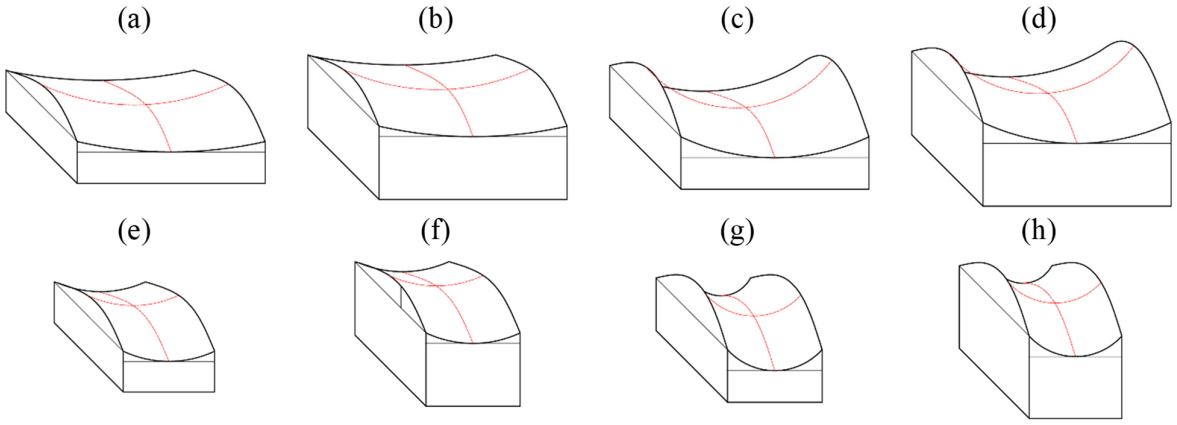

Figure 1. Geometry of the considered physical models: (a) SLF, (b) SHF, (c) SLC, (d) SHC, (e) RLF, (f) RHF, (g) RLC, and (h) RHC.

This paper investigates the eight building geometries characterized by the three

following parameters, namely: (1) plan shapes, i.e., square (S) and rectangular (R) shapes; (2) building heights, i.e., higher (H) and lower (L) buildings; and (3) roof curvatures, i.e., low curvature or flatter (F) and high curvature or more curved (C). Thus, each geometry is identified by an acronym made of three letters that identify the building plan shape (S or R), the building height (H or L), and the roof curvature (F or C), respectively. Figure 1 shows the eight geometries with the corresponding acronyms, whereas Figure 2 illustrates the geometrical parameters used to define the different models and the corresponding wind angles of attack. In particular, L_1 and L_2 denote the sagging (upward curvature) and the hogging (downward curvature) spans, f_1 and f_2 are the sagging and hogging sags, H_1 is the height of the lowest roof point, and H_2 is the height of the highest roof point. Table 1 summarizes the geometric properties of the different physical models.

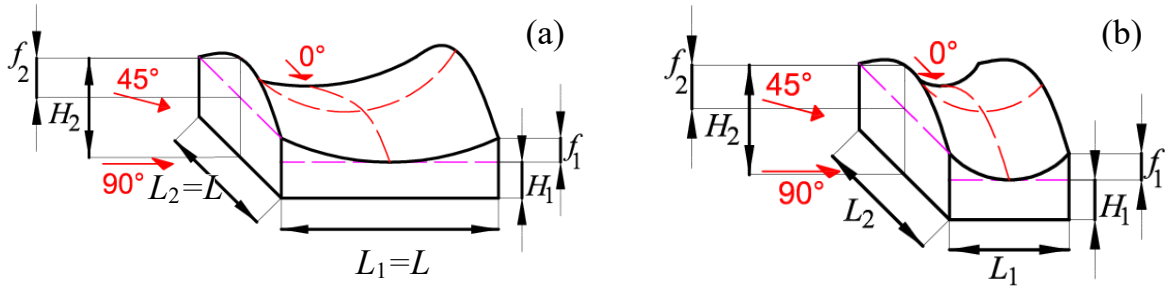

Figure 2. Definition of the geometrical parameters for the hyperbolic paraboloid models and of the wind angles of attack: (a) square plan models, and (b) rectangular plan models.

Table 1. Geometric properties of the physical models (dimensions in mm).

	L_1	L_2	f_1	f_2	H_1	H_2
SLF	800	800	27	53	133	213
SHF	800	800	27	53	267	347
SLC	800	800	44	89	133	267
SHC	800	800	44	89	267	400
RLF	400	800	27	53	133	213
RHF	400	800	27	53	267	347
RLC	400	800	44	89	133	267
RHC	400	800	44	89	267	400

Figure 3 shows a picture of the four physical models corresponding to the lower building configuration. It is noted here that the four physical models corresponding to the

higher building configuration were obtained from those shown in Figure 4 by adding under their bottom a rectangular parallelepiped base of dimensions 800 mm x 800 mm x 133 mm for the square shapes, and 400 mm x 800mm x 133 mm for the rectangular shapes.

Figure 3. Physical models (from left to right: RLC, RLF, SLF, and SLC).

Figure 4 shows pictures of the eight physical models during the wind tunnel test (Rizzo et al. 2011, Rizzo 2014). The insets in Figure 4 show the geometry and the acronym corresponding to each physical model. Figure 4 also illustrate the cubic wooden elements used to reproduce the appropriate roughness and, in conjunction with the upstream shark fins, to simulate the desired turbulence for the atmospheric boundary layer flow in the wind tunnel. In the wind tunnel used for these tests, the air flow is produced by suction through fans located downstream of the test section.

The wind tunnel blockage ratios observed in the tests assumed values in the range between 1.5% and 7.7%, and required the application of correction values to the pressure coefficients ranging from a minimum of 2% to a maximum of 4%. The wind tunnel test results for three wind attack angles (θ), namely θ = 0°, 45°, and 90°, are considered in the present study. It is noteworthy that the full experimental results included 16 different wind attack angles in the range from 0° to 360°, and that the wind pressure coefficients for θ = 22.5° and 67.5° were also meaningful, due to the doubly-symmetric plan geometry of the physical models. However, the angles θ = 0°, 45° and 90° were selected here due to space limitations and because they were previously identified as the most important in describing the wind pressure coefficients for the given geometries (in fact, the wind pressure coefficients for θ =

22.5° were qualitatively similar to those for θ = 0°, and the wind pressure coefficients for θ = 67.5° were qualitatively similar to those for θ = 45°) (Rizzo et al. 2011).

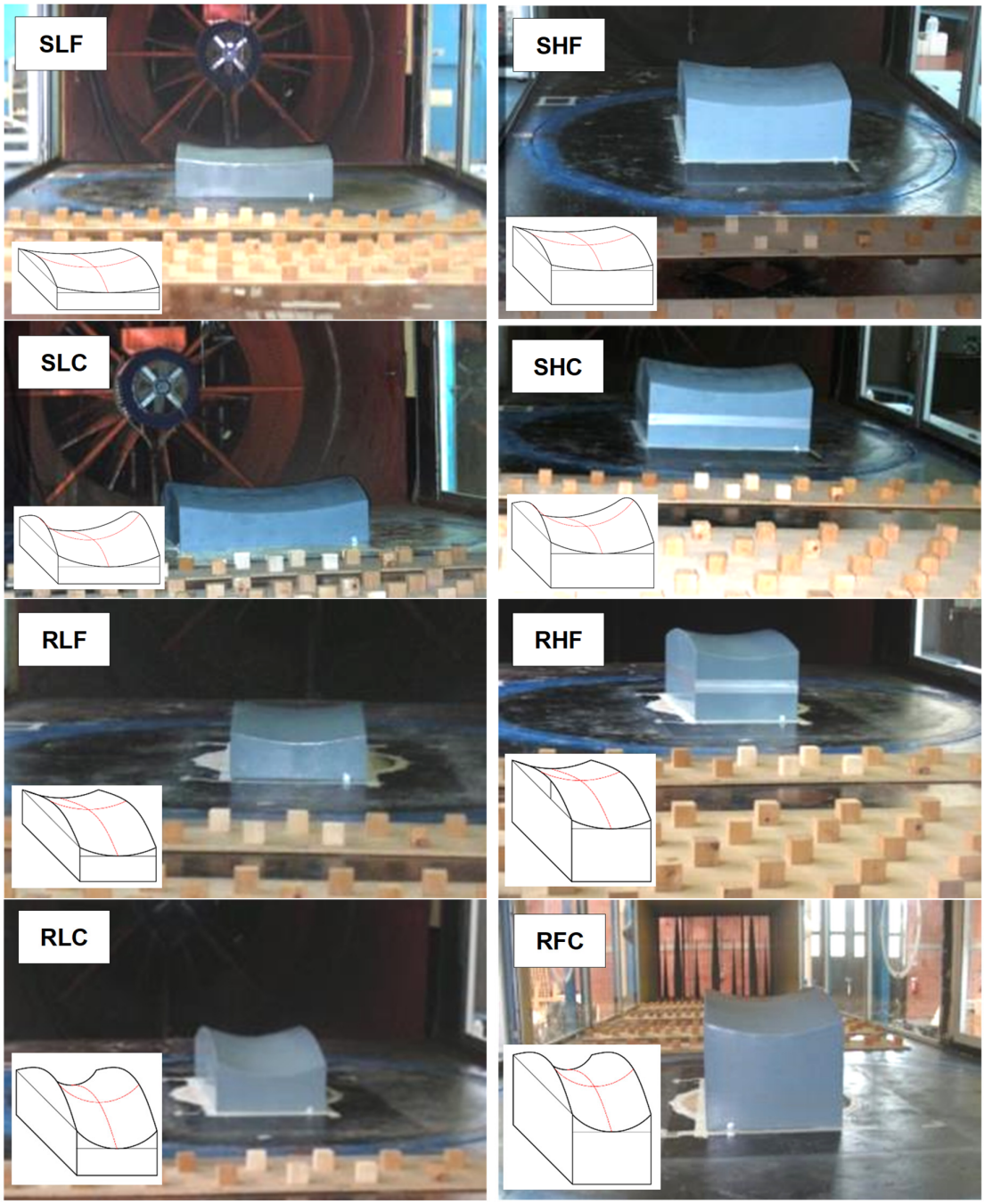

Figure 4. Physical models in the wind tunnel.

Pressure taps were distributed on the roof models as illustrated in Figure 5. The number of pressure taps used on roof models with a square plan was 89, whereas the number

of pressure taps used on roof models with rectangular plan was 95. Figure 5 also identifies five different relevant regions of the roofs, referred to as regions A through E, respectively. Zone A is the edge detachment zone for θ = 0°, zone B is the edge detachment zone for θ = 90°, zone C represents the roof edge parallel to zone B, zone D represents the roof edge parallel to zone A, and zone E is in the central portion of the roof.

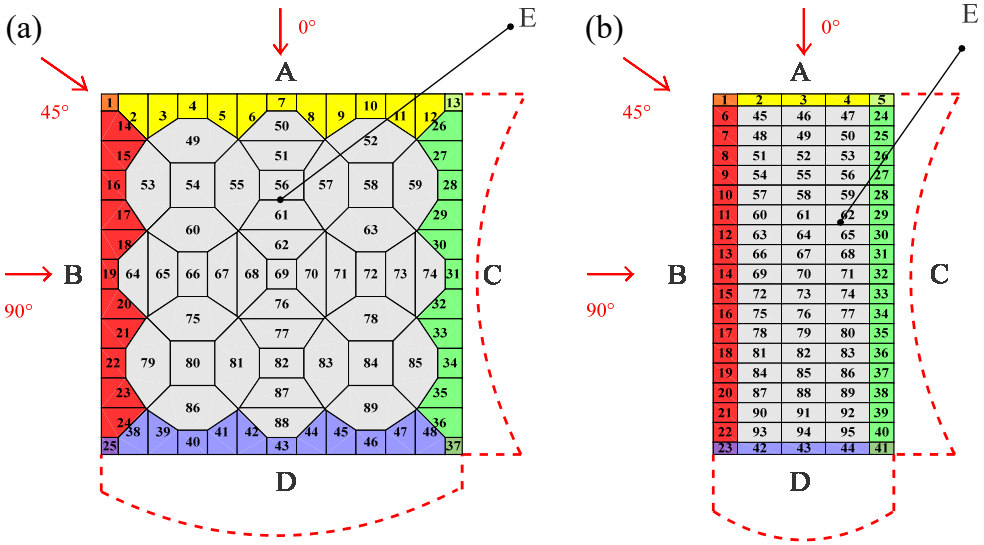

Figure 5. Pressure tap distributions on physical roof models: (a) square models, (b) rectangular models.

4. STATISTICAL CHARACTERIZATION OF EXPERIMENTAL PRESSURE COEFFICIENTS

The first phase of the investigation reported here focuses on the statistical characterization of the pressure coefficients as defined in (Rizzo et al. 2011) and measured at different locations of the considered roof geometries through wind tunnel tests (Rizzo et al. 2011). The following relevant pressure coefficient statistics are analyzed hereinafter: (1) mean, μ_{c_p}; (2) standard deviation, σ_{c_p}; (3) skewness coefficient, γ_{c_p}; (4) excess kurtosis, κ_{c_p}; and (5) mean zero-crossing rate, ν_0. In this study, positive pressure coefficient values correspond to suction (negative pressure when compared to the atmospheric pressure). The statistics of the experimental results are calculated considering the entire duration of the

experiments, i.e., for T_0 = 29.77 s, under the assumption of stationarity for the underlying stochastic processes. With the exceptions of pressure coefficient mean and standard deviations, all calculations were performed on the normalized and standardized signals (i.e., zero-mean processes with unit standard deviation), as suggested in Kwon and Kareem (2011).

It is highlighted here that the values of skewness coefficient, excess kurtosis, and mean zero-crossing rate are necessary for the calculation of the wind pressure PF statistics when using analytical models such as those considered in this study.

Table 2 through Table 7 report the maximum and minimum values of the considered statistics over each roof zone (i.e., A through E) for square and rectangular plan models and θ = 0°, 45°, and 90° wind angles of attack. The results reported in these tables indicate that the mean pressure is always positive (i.e., negative average pressure corresponding to a suction force), with the exception of the RLF model for angles θ = 0° and 45°, for which some pressure taps have negative mean pressure coefficients (i.e., positive average pressures).

4.1 Square plan model pressure coefficient statistics for θ = 0°

Table 2 reports the experimental pressure coefficient statistics for models with square plan and θ = 0°. The mean pressure coefficients, μ_{c_p}, vary significantly among different models and within different roof regions of the same model (Rizzo et al. 2011).

The μ_{c_p} values are highest in zone A (detachment zone), with maximum values ranging from 1.893 (SHF) to 0.884 (SLC), whereas they are lowest in zone D. Generally, within the same roof zones, the higher curvature roofs exhibit lower mean pressure coefficients than the flatter roofs, and the higher building models present higher mean pressure coefficients. The standard deviations of the pressure coefficients, σ_{c_p}, reach their maximum values in zone A for all square plan models, with values contained between 0.532 (SHC) and 0.357 (SLC).

The higher building models (SHF and SHC) present higher maximum values of σ_{c_p} when compared with the corresponding lower building models (SLF and SLC).

Table 2. Statistics of pressure coefficients for square plan and θ = 0°.

Zone	Model	Max/Min	μ_{c_p}	σ_{c_p}	γ_{c_p}	κ_{c_p}	ν_0 (Hz)
A	SLF	Max	1.332	0.363	0.706	0.930	12.529
		Min	0.555	0.140	0.329	0.257	11.051
	SHF	Max	1.893	0.414	0.686	1.500	14.646
		Min	0.819	0.163	0.295	0.031	12.529
	SLC	Max	0.884	0.357	0.802	1.312	13.672
		Min	0.582	0.061	0.078	-0.169	7.457
	SHC	Max	1.463	0.532	0.334	0.420	11.891
		Min	0.883	0.063	-0.536	-0.314	5.811
B	SLF	Max	0.563	0.155	1.417	7.236	14.243
		Min	0.263	0.049	0.069	-0.374	8.163
	SHF	Max	0.819	0.163	1.943	10.126	15.519
		Min	0.263	0.092	0.103	0.044	10.951
	SLC	Max	0.661	0.126	1.161	3.278	15.284
		Min	0.263	0.053	0.103	0.116	11.958
	SHC	Max	1.017	0.159	2.162	10.766	15.452
		Min	0.263	0.081	0.103	0.116	11.051
C	SLF	Max	0.706	0.211	1.486	6.495	14.713
		Min	0.266	0.047	0.136	-0.028	10.480
	SHF	Max	1.146	0.326	2.638	19.963	15.855
		Min	0.333	0.076	0.158	0.107	10.984
	SLC	Max	0.579	0.125	0.815	1.942	16.661
		Min	0.175	0.057	0.064	-0.036	12.093
	SHC	Max	0.910	0.149	1.659	8.545	17.199
		Min	0.266	0.076	-0.129	0.042	10.951
D	SLF	Max	0.343	0.059	0.225	0.541	12.597
		Min	0.192	0.042	-0.033	-0.063	8.666
	SHF	Max	0.606	0.094	0.601	1.818	15.687
		Min	0.309	0.048	-0.535	0.090	7.692
	SLC	Max	0.415	0.078	0.467	0.762	14.847
		Min	0.104	0.034	-0.192	-0.059	11.051
	SHC	Max	0.710	0.095	0.428	0.797	14.814
		Min	0.247	0.043	-0.248	-0.031	9.070
E	SLF	Max	0.591	0.095	1.261	3.926	12.597
		Min	0.330	0.040	-0.098	-0.374	7.659
	SHF	Max	0.813	0.273	1.482	4.077	14.478
		Min	0.412	0.039	-0.359	-0.208	7.558
	SLC	Max	1.004	0.298	0.673	1.143	14.982
		Min	0.193	0.041	-0.218	-0.326	5.912
	SHC	Max	1.472	0.502	0.235	0.687	12.261
		Min	0.236	0.052	-0.452	-0.323	5.475

The skewness coefficient and the excess kurtosis show a very similar trend for all geometries, assuming high positive values in the middle of zones B and C. The skewness coefficients assume higher values for higher models and for flatter roof values. The excess kurtosis follow the same trend as the skewness coefficients and assume their highest value

of 19.963 for the SHF model in zone C.

All square plan roofs present skewness coefficients and excess kurtosis values greater than 0.5 in zones A, B, and C, which is an indication of non-Gaussian behavior according to Suresh Kumar and Stathopoulos (2000). The mean zero-crossing rates, ν_0, present significant differences between lower and higher curvature roofs, particularly in zones A, D and E. In zone A, model SLC has ν_0 values between 7.457 Hz and 13.672 Hz, whereas model SLF presents values between 11.051 Hz and 12.529 Hz. In zones D and E, the trend is opposite, i.e., lower curvature roofs show greater $\nu_0$variability than higher curvature roofs.

Although a symmetrical behavior would be expected for roof zones that are symmetrical with respect to the wind direction, slight differences are observed in the experimental values of the pressure coefficient statistics in correspondence of θ = 0° and θ = 90°. These differences are most likely due to a combination of model imperfections, small variations in the pressure tap positions, imperfections in the wind flow, and inherent variability in samples of stochastic processes.

4.2 Rectangular plan model pressure coefficient statistics for θ = 0°

Table 3 reports the experimental pressure coefficient statistics for models with rectangular plan and θ = 0°. In general, the mean pressure coefficients for rectangular plan roofs are significantly smaller than those for the corresponding square plan roofs (Rizzo et al. 2011). This result may be explained by larger sag-to-length ratio in the across-wind direction for rectangular plans when θ = 0°, which likely implies a greater confinement of the wind flow when compared to the case of square plan roofs.

The highest mean pressure coefficients are achieved in zone A (detachment zone) for models RLF, RHF, and RHC, and in zone E for model RLC. Zones B, C, and E all experience relatively high values of μ_{c_p}, particularly zone E close to zone A. Zone D exhibits the lowest

values of μ_{c_p} for all rectangular plan geometries.

Table 3. Statistics of pressure coefficients for rectangular plan and θ = 0°.

Zone	Model	Max/Min	μ_{c_p}	σ_{c_p}	γ_{c_p}	κ_{c_p}	ν_0 (Hz)
A	RLF	Max	0.716	0.284	0.595	0.553	12.597
		Min	0.253	0.096	0.109	0.037	3.124
	RHF	Max	1.416	0.363	0.581	0.942	13.839
		Min	0.534	0.124	0.149	-0.334	2.990
	RLC	Max	0.246	0.297	0.610	1.065	14.041
		Min	0.097	0.098	0.268	0.122	9.842
	RHC	Max	0.990	0.398	0.762	1.458	14.007
		Min	0.335	0.101	-0.299	0.124	11.219
B	RLF	Max	0.314	0.096	1.069	2.727	13.369
		Min	0.138	0.044	0.168	0.232	11.085
	RHF	Max	0.593	0.132	2.163	17.706	13.772
		Min	0.233	0.058	0.083	0.116	10.077
	RLC	Max	0.627	0.129	1.322	4.431	15.150
		Min	0.125	0.052	0.047	-0.348	8.532
	RHC	Max	0.759	0.136	1.497	5.882	15.082
		Min	0.216	0.043	0.065	-0.071	9.977
C	RLF	Max	0.340	0.096	1.069	2.861	15.250
		Min	0.116	0.037	-0.088	-0.126	10.212
	RHF	Max	0.593	0.132	2.371	21.778	15.519
		Min	0.231	0.046	-0.043	0.010	5.072
	RLC	Max	0.583	0.129	1.230	3.544	15.150
		Min	0.145	0.047	-0.033	-0.087	9.708
	RHC	Max	0.688	0.136	1.649	7.193	15.989
		Min	0.236	0.048	0.117	0.050	9.607
D	RLF	Max	0.194	0.103	1.263	3.602	12.194
		Min	0.112	0.037	0.040	-0.126	9.204
	RHF	Max	0.635	0.329	0.817	0.288	11.152
		Min	0.256	0.046	-0.043	-0.237	9.070
	RLC	Max	0.211	0.097	0.086	0.662	13.369
		Min	-0.076	0.047	-0.158	-0.200	9.708
	RHC	Max	0.268	0.143	1.223	3.098	12.026
		Min	0.082	0.048	-0.003	0.070	9.405
E	RLF	Max	0.357	0.096	1.069	2.727	13.772
		Min	0.107	0.034	-0.196	-0.299	9.002
	RHF	Max	0.619	0.296	1.581	5.230	14.948
		Min	0.231	0.038	-0.175	-0.170	8.633
	RLC	Max	0.659	0.076	0.220	0.296	13.369
		Min	0.037	0.039	-0.258	-0.401	6.853
	RHC	Max	0.897	0.119	0.763	2.668	12.865
		Min	0.082	0.040	-0.185	-0.167	6.550

Pressure coefficient standard deviations assume values of similar magnitude of those for the corresponding square plan models. The maximum values are generally reached in zone A, with the highest maximum value equal to 0.398 for model RHC; the minimum values are measured in zone E for all geometries, with the lowest minimum value equal to 0.034 for model RLF. Skewness coefficients and excess kurtosis follow similar trends as those

observed for the corresponding square plan models, i.e., they assume their highest values in zones B and C. The highest skewness coefficient value is equal to 2.371 and is measured in zone C for model RHF, whereas the lowest value is equal to -0.299 and is observed in zone

A for model RHC. Everything else being the same, the lower curvature roofs have higher skewness coefficient values than the higher curvature models. Excess kurtosis values are generally higher than for the corresponding square plan models, with the largest maximum value equal to 21.778 for RHF in zone C. Based on the threshold value of 0.5 for the absolute values of skewness coefficients and excess kurtosis Chilton (2010), most of the pressure coefficients records in zones A, B, and C can be considered non-Gaussian.

The mean zero-crossing rates exhibit a greater variability within each roof zone than for the corresponding square plan models. In fact, the highest ν_0 value is equal to 15.519 Hz (measured for model RHF in zone C), whereas the smallest ν_0 value is equal to 2.990 Hz (measured for model RHF in zone A).

4.3 Square plan model pressure coefficient statistics for θ = 45°

Table 4 reports the experimental pressure coefficient statistics for models with square plan and θ = 45°. The mean pressure coefficients for θ = 45° are generally higher than those for θ = 0°, ranging between 2.632 (model SHC, zone B) and 0.161 (model SLF, zones D and E). The highest values are observed in the detachment zones A and B, and in some parts of zone E that are very close to the detachment zones (Rizzo et al. 2011).

Higher building models have significantly higher mean pressure coefficient values than lower building models in all zones, whereas lower curvature roof models have slightly higher mean pressure coefficient values than higher curvature roofs in zones A and B. The standard deviations of the pressure coefficients reaches their highest values in zones A, B, and in parts of zone E, with the maximum value equal to 0.772 (model SHC, zone E). Skewness

coefficients assume values larger than 0.5 in absolute value in several locations of all zones for all geometries. The skewness coefficient highest values are located in: zone E for model SLF (γ_{c_p} = 1.299), zone D for model SHF (γ_{c_p} = 1.528), and zone C for models SLC (γ_{c_p} = 1.215) and SHC (γ_{c_p} = 1.336). The lowest values are observed in zone E for models SLF (γ_{c_p} = -0.529), SHF (γ_{c_p}= -0.580), and SLC (γ_{c_p}= -0.533), and in zone A for model SHC (γ_{c_p} = -0.575).

Table 4. Statistics of pressure coefficients for square plan and θ = 45°.

Zone	Model	Max/Min	μ_{c_p}	σ_{c_p}	γ_{c_p}	κ_{c_p}	ν_0 (Hz)
A	SLF	Max	1.363	0.333	0.730	1.242	14.746
		Min	0.552	0.085	0.274	0.130	10.312
	SHF	Max	2.374	0.426	0.842	2.618	16.628
		Min	0.864	0.131	-0.097	-0.295	9.741
	SLC	Max	1.291	0.341	0.728	1.293	11.790
		Min	0.295	0.046	0.068	0.027	10.581
	SHC	Max	2.344	0.443	0.599	0.611	13.873
		Min	0.810	0.050	-0.575	-0.128	10.380
B	SLF	Max	1.607	0.333	1.184	2.107	16.325
		Min	0.490	0.064	0.071	0.130	10.312
	SHF	Max	2.374	0.426	1.184	2.107	19.214
		Min	0.510	0.196	-0.071	-0.134	11.152
	SLC	Max	1.819	0.341	1.184	2.107	18.811
		Min	0.510	0.156	0.071	-0.053	10.816
	SHC	Max	2.632	0.443	1.184	2.107	17.400
		Min	0.510	0.179	-0.047	-0.300	10.380
C	SLF	Max	0.765	0.130	0.672	4.744	15.150
		Min	0.481	0.061	0.024	0.166	13.134
	SHF	Max	1.200	0.196	1.527	4.705	19.214
		Min	0.662	0.073	-0.182	0.368	12.731
	SLC	Max	0.863	0.198	1.215	3.537	18.811
		Min	0.460	0.051	-0.175	0.249	10.917
	SHC	Max	1.255	0.222	1.336	13.534	17.400
		Min	0.714	0.063	-0.090	-0.171	8.734
D	SLF	Max	0.820	0.110	0.587	1.919	15.150
		Min	0.161	0.050	-0.203	-0.113	10.380
	SHF	Max	0.995	0.162	1.528	4.705	17.131
		Min	0.692	0.086	-0.217	0.031	8.734
	SLC	Max	0.817	0.138	0.665	2.080	15.855
		Min	0.426	0.063	-0.108	-0.033	12.294
	SHC	Max	1.156	0.149	0.701	2.432	15.855
		Min	0.689	0.096	-0.120	-0.033	8.196
E	SLF	Max	1.290	0.483	1.299	3.823	13.336
		Min	0.161	0.034	-0.529	-0.601	9.943
	SHF	Max	2.311	0.620	1.138	5.339	15.989
		Min	0.305	0.034	-0.580	-0.349	7.356
	SLC	Max	1.621	0.575	0.815	3.055	14.310
		Min	0.182	0.040	-0.533	-0.656	6.886
	SHC	Max	2.685	0.772	0.704	1.708	16.896
		Min	0.452	0.040	-0.465	-0.416	7.256

The excess kurtosis follow similar trends as the skewness coefficients, i.e., a high excess kurtosis value generally corresponds to a high skewness coefficient value. The maximum excess kurtosis value is equal to 13.534 (model SHC, zone C), whereas the minimum is equal to -0.656 (model SLC, zone E). Negative excess kurtosis values are observed in several pressure taps in zones A, B, D, and E for all models, as well as a few pressure taps in zone C for model SHC. It has also been observed that the pressure coefficient processes are non-Gaussian in most of the pressure taps in zones A, B, and C, as well as in a non-negligible portion of D and E. The mean zero-crossing rates assume larger values around the edges in zones A, B, and C, and in parts of zone E. The highest mean zero-crossing rate value is 19.214 Hz (model SHF, zone C), and the lowest is 7.256 Hz (model SHC, zone E).

4.4 Rectangular plan model pressure coefficient statistics for θ = 45°

Table 5 reports the experimental pressure coefficient statistics for models with rectangular plan and θ = 45°. For this wind angle, rectangular plan models have mean pressure coefficients that are higher than those of the corresponding square models; thus, they follow the opposite trend than that observed for θ = 0° (Rizzo et al., 2011). The highest value is 3.497 for model RHF in zone A, which is significantly higher than the 2.374 value for SHF in zone A. The lowest values are observed in zone D and part of zone E. Few pressure taps in these two zones of model RLC present negative mean pressure coefficient values. These negative values are due to irregular vortex shedding.

The highest values of the pressure coefficient standard deviations are observed in zones A and B and in some parts of zone E for all models, with the maximum value equal to 0.686 (model RHF, zones A and B). The skewness coefficient and excess kurtosis values

are larger than 0.5 in absolute value in most of the pressure taps for all models. Overall, the values of the skewness coefficients and excess kurtosis are higher for the rectangular plan models than for the corresponding square plan models. The highest skewness coefficient value is equal to 2.440 (zones A and B of model RHC).

Table 5. Statistics of pressure coefficients for rectangular plan and θ = 45°.

Zone	Model	Max/Min	μ_{c_p}	σ_{c_p}	γ_{c_p}	κ_{c_p}	ν_0 (Hz)
A	RLF	Max	1.472	0.413	0.722	1.643	13.739
		Min	0.264	0.074	0.243	0.036	3.460
	RHF	Max	3.497	0.686	0.498	0.797	13.336
		Min	0.651	0.113	-0.073	-0.119	3.493
	RLC	Max	1.946	0.558	1.611	6.495	13.470
		Min	0.163	0.101	0.238	0.135	10.850
	RHC	Max	0.959	0.390	2.440	7.866	14.007
		Min	0.076	0.131	0.131	-0.174	10.447
B	RLF	Max	1.472	0.413	1.479	4.442	18.374
		Min	0.138	0.101	0.327	0.193	10.951
	RHF	Max	3.496	0.686	1.547	3.986	18.878
		Min	0.608	0.110	-0.119	-0.110	9.238
	RLC	Max	1.946	0.558	1.230	4.122	20.155
		Min	0.223	0.073	0.084	0.030	11.051
	RHC	Max	2.110	0.306	2.440	7.866	16.325
		Min	0.076	0.094	-0.926	-0.788	10.380
C	RLF	Max	0.626	0.101	0.629	2.056	15.217
		Min	0.138	0.064	-0.075	0.115	9.540
	RHF	Max	1.260	0.142	0.577	0.856	15.889
		Min	0.505	0.099	-0.398	0.051	2.822
	RLC	Max	0.668	0.231	1.837	8.919	17.534
		Min	0.389	0.065	0.143	0.129	10.648
	RHC	Max	0.966	0.336	0.678	1.244	19.953
		Min	0.535	0.066	-0.148	-0.041	11.488
D	RLF	Max	0.453	0.128	1.774	6.599	14.746
		Min	0.111	0.071	0.291	0.380	10.917
	RHF	Max	0.652	0.233	1.655	8.377	15.889
		Min	0.306	0.085	0.118	0.064	11.287
	RLC	Max	0.664	0.116	1.163	3.890	15.317
		Min	-0.016	0.068	0.265	0.228	9.876
	RHC	Max	0.557	0.193	1.264	2.659	12.630
		Min	0.030	0.066	0.145	-0.041	10.648
E	RLF	Max	0.954	0.330	1.858	29.640	15.620
		Min	0.034	0.048	-0.454	-0.371	10.010
	RHF	Max	1.617	0.475	1.560	5.024	17.031
		Min	0.123	0.054	-0.422	-0.569	10.111
	RLC	Max	1.706	0.451	1.915	6.874	17.299
		Min	-0.062	0.067	-0.124	-0.486	9.473
	RHC	Max	1.043	0.137	0.766	2.416	13.873
		Min	0.030	0.041	-0.283	-0.157	8.532

Generally, the higher curvature models present higher skewness coefficient values than the corresponding lower curvature roofs, except for a few cases in zones B and D for

the lower building models (RLF and RLC). The excess kurtosis attains its highest value of 29.640 in zone E for model RLC, and its minimum value of -0.788 in zone B for model RHC. The mean zero-crossing rates assume larger values along the edges (zones A, B, and C) and near the corners in zones D and E. The observed values are similar to those of the corresponding square models, ranging between 20.155 (model RLC, zone B) and 3.493 (model RHF, zone A).

4.5 Square plan model pressure coefficient statistics for θ = 90°

Table 6 reports the experimental pressure coefficient statistics for models with square plan and θ = 90°. Mean pressure coefficients are lower for this angle than they are for θ = 45°, although many pressure taps present higher vales than for θ = 0° (Rizzo et al. 2011). The maximum values are achieved in zone B for model SLF ($\mu_{c_p} = 1.426$), in zones C and D for model SHF ($\mu_{c_p} = 1.576$), in zone A for model SLC ($\mu_{c_p} = 1.184$), and in zone E for model SHC ($\mu_{c_p} = 1.482$). However, in average, the mean pressure values are higher in zone B (detachment zone) than in other zones for all models. Also in average, the higher curvature roofs present lower mean pressure coefficients than lower curvature roofs for the same model height, and higher building models have higher mean pressure coefficients than lower building models for the same roof curvature.

Mean pressure coefficients decrease less sharply from the detachment zone (zone B) to the middle zone (zone E) than they do for θ = 0°, and then increase slightly from zone E to zone C (i.e., the edge opposite to the wind direction). In average, the standard deviations of the pressure coefficients assume larger values in zones A and D (i.e., the edges parallel to the wind direction) than in other zones, and range between 0.422 (model SHF in zone D) and 0.052 (model SLF in zone C). The values of the pressure coefficient standard deviations are similar, within each zone, between models of different height and different roof curvature.

The highest values of the skewness coefficients are observed in zones A, B, D, and the portion of E that is closest to B.

Table 6. Statistics of pressure coefficients for square plan and θ = 90°.

Zone	Model	Max/Min	μ_{c_p}	σ_{c_p}	γ_{c_p}	κ_{c_p}	ν_0 (Hz)
A	SLF	Max	1.410	0.387	0.858	3.220	15.620
		Min	0.134	0.064	0.021	-0.054	8.599
	SHF	Max	1.467	0.381	1.163	3.100	16.863
		Min	0.228	0.079	0.162	0.536	8.297
	SLC	Max	1.184	0.345	1.208	3.967	16.695
		Min	0.159	0.089	-0.235	-1.817	10.178
	SHC	Max	1.426	0.358	1.417	4.432	16.124
		Min	0.478	0.167	0.122	0.391	9.741
B	SLF	Max	1.426	0.346	1.454	5.345	12.227
		Min	0.428	0.065	-0.022	0.213	8.566
	SHF	Max	1.466	0.321	1.901	8.275	10.279
		Min	1.128	0.212	0.841	1.558	8.129
	SLC	Max	1.079	0.233	2.234	17.664	10.883
		Min	0.859	0.200	0.931	1.792	9.372
	SHC	Max	1.356	0.205	1.332	9.192	11.555
		Min	1.138	0.169	0.580	1.093	9.271
C	SLF	Max	1.057	0.269	0.461	0.862	12.664
		Min	0.382	0.052	-0.130	-0.143	8.095
	SHF	Max	1.576	0.422	1.229	2.251	12.697
		Min	0.435	0.067	-0.057	-0.106	8.129
	SLC	Max	1.164	0.343	1.009	2.091	13.705
		Min	0.313	0.064	-0.199	0.001	9.372
	SHC	Max	1.393	0.311	1.041	3.967	15.183
		Min	0.497	0.086	-0.006	0.002	9.607
D	SLF	Max	1.057	0.269	0.583	1.899	16.191
		Min	0.203	0.068	0.126	0.309	11.522
	SHF	Max	1.576	0.422	0.983	4.843	16.023
		Min	0.251	0.067	0.067	0.032	10.548
	SLC	Max	1.026	0.264	1.253	5.374	15.519
		Min	0.164	0.064	0.026	0.001	9.909
	SHC	Max	1.415	0.365	1.136	3.944	15.855
		Min	0.289	0.086	0.157	0.164	11.488
E	SLF	Max	1.053	0.268	0.618	1.254	15.519
		Min	0.090	0.085	-0.249	0.067	10.951
	SHF	Max	1.412	0.296	0.915	2.393	16.527
		Min	0.150	0.071	-0.149	0.028	11.488
	SLC	Max	1.062	0.265	0.999	2.584	15.485
		Min	0.056	0.082	-0.253	0.075	8.700
	SHC	Max	1.482	0.327	1.457	5.279	16.224
		Min	0.124	0.144	-0.382	-0.056	8.499

Most pressure taps have values larger than 0.5, suggesting that for θ = 90° the non-Gaussian zone is larger than for θ = 0°. The highest value is equal to 2.234 (model SLC in zone B), whereas the lowest is -0.382 (model SHC in zone E). Higher curvature roofs generally have higher skewness coefficient values than lower curvature roofs, except for the

higher building models (i.e., SHF and SHC) in zones B and C. The excess kurtosis values follow a similar trend to that of the skewness coefficients, with the highest value equal to 17.664 observed in zone B of model SLC, and the lowest value equal to -1.817 observed in zone A of model SLC. The mean zero-crossing rates, on average, assume higher values than for other wind angles, ranging from 16.863 Hz (model SHF in zone A) to 8.499 Hz (model SHC in zone E).

4.6 Rectangular plan model pressure coefficient statistics for θ = 90°

Table 7 reports the experimental pressure coefficient statistics for models with rectangular plan and θ = 90°. Mean pressure coefficients are generally smaller than for θ = 45° and higher than for θ = 0°. The highest values are observed in the detachment zone (zone B), with a maximum value equal to 2.296 for model RHC. Large parts of the roofs experience high suction values. All pressure taps have positive mean pressure coefficient values. The lowest values are observed in zone E in the center of the roof, with a minimum value equal to 0.231 for model RLF. The standard deviations of the pressure coefficients range from 0.565 (model RHC in zone E) to 0.064 (model RHC in zone C), with relatively small variations (i.e., smaller than for the models with square plans) between the edges and the center of the roof. Values are closer in each zone than with the square plan.

Higher models show generally higher values than lower ones, whereas the differences in roof curvature do not affect significantly the values of the pressure coefficient standard deviations. The skewness coefficients show an asymmetry between zones A and D (i.e., edges parallel to the wind flow), with the skewness coefficient values that are systematically higher in zone A than in zone D. The excess kurtosis values also present this anomalous asymmetry, which is not observed for the mean pressure coefficients and is less evident for the PFs.

Table 7. Statistics of pressure coefficients for rectangular plan and θ = 90°.

Zone	Model	Max/Min	μ_{c_p}	σ_{c_p}	γ_{c_p}	κ_{c_p}	ν_0 (Hz)
A	RLF	Max	0.918	0.216	1.523	5.039	15.889
		Min	0.239	0.100	0.336	0.750	3.393
	RHF	Max	1.331	0.331	1.380	5.256	17.064
		Min	0.563	0.124	0.280	0.432	3.023
	RLC	Max	1.126	0.302	1.356	4.611	13.403
		Min	0.525	0.168	-0.337	0.415	11.858
	RHC	Max	1.165	0.225	1.038	4.116	18.744
		Min	0.862	0.151	0.067	0.009	12.529
B	RLF	Max	0.998	0.277	1.779	9.346	14.646
		Min	0.231	0.158	0.022	0.184	10.951
	RHF	Max	1.406	0.333	2.079	11.865	16.527
		Min	0.524	0.142	0.423	0.910	9.338
	RLC	Max	1.180	0.290	1.266	4.431	16.124
		Min	0.385	0.127	0.369	1.105	9.641
	RHC	Max	2.296	0.346	0.526	1.578	19.651
		Min	0.691	0.171	0.113	0.373	14.746
C	RLF	Max	0.823	0.217	0.620	4.010	16.997
		Min	0.175	0.078	-0.229	0.184	13.772
	RHF	Max	1.384	0.347	1.103	3.473	16.527
		Min	0.379	0.067	0.170	0.451	6.584
	RLC	Max	1.149	0.319	0.816	2.097	16.628
		Min	0.307	0.117	0.088	0.339	12.395
	RHC	Max	1.177	0.196	0.379	1.886	16.628
		Min	0.616	0.068	-0.040	0.009	11.656
D	RLF	Max	0.824	0.202	0.456	1.429	16.426
		Min	0.231	0.155	0.022	0.184	12.731
	RHF	Max	1.305	0.347	0.576	1.012	14.377
		Min	0.510	0.249	-0.091	0.111	11.085
	RLC	Max	1.114	0.319	0.925	2.443	14.343
		Min	0.342	0.205	-0.337	0.415	10.816
	RHC	Max	1.596	0.553	0.374	0.463	16.628
		Min	0.701	0.113	-0.018	-0.255	12.529
E	RLF	Max	0.869	0.247	0.569	1.616	15.150
		Min	0.231	0.170	-0.342	0.181	11.891
	RHF	Max	1.379	0.377	0.949	2.760	13.705
		Min	0.487	0.210	-0.268	0.105	11.354
	RLC	Max	1.169	0.295	0.948	2.830	13.470
		Min	0.308	0.153	-0.497	0.124	10.951
	RHC	Max	2.838	0.565	1.927	6.727	16.628
		Min	0.391	0.064	-0.076	-0.306	11.186

The skewness coefficients assume their highest value in zone B, with a maximum value of 2.079 for model RHF, and their lowest value in zone E, with a minimum value of -0.497 for model RLC. The excess kurtosis follows the same trend as the skewness coefficient, reaching its highest value of 11.865 in zone B of model RHF, and its lowest value

of -0.306 in zone E of model RHC.

The excess kurtosis does not follow a uniform trend between higher and lower models or higher and lower curvature models for all roof regions. However, the lower curvature roofs exhibit significantly higher values of the excess kurtosis in zone B, when compared to the corresponding higher curvature models. The mean zero-crossing rates range from 3.023 Hz (in zone A of model RHF) to 19.651 Hz (in zone B of model RHC). This range is significantly wider than for square plan models and θ = 90°.

4.7 Synoptic considerations on Gaussianity of pressure coefficient process

This section summarizes the results in terms of non-Gaussianity of pressure coefficient processes among the eight different physical models and the three wind angles of attack based on the criteria suggested in Suresh Kumar and Stathopoulos (2000), i.e., $\left|\gamma_{c_p}\right| > 0.5$ or $\left|\kappa_{c_p}\right| > 0.5$. In particular, Table 8 shows the percentage of pressure taps for each of the models and the three wind angles of attack where the skewness coefficient, γ_{c_p}, the excess kurtosis, κ_{c_p}, and at least one between skewness coefficient or excess kurtosis is larger than 0.5 in absolute value. Table 8 also provides the averages of these percentages over all models for a given wind angle of attack.

For any given physical model and wind angle of attack, the number of pressure taps with large absolute values of the excess kurtosis is higher than that with large absolute values of the skewness coefficient. This result suggests that, for HPRs, non-Gaussianity is controlled mainly by the excess kurtosis. It is observed that, among the parameters considered in this study, the wind angle of attack has the largest effect on the percentage of non-Gaussianity. In fact, the average percentage of non-Gaussian pressure taps' records (i.e., for which at least one between skewness and excess kurtosis coefficient is larger than 0.5 in absolute

value) is equal to 29.0%, 38.4%, and 68.9% for θ = 0°, 45° and 90°, respectively.

Table 8. Percentage of pressure taps corresponding to non-Gaussian conditions.

Model	$\lvert\gamma_{c_p}\rvert > 0.5$			$\lvert\kappa_{c_p}\rvert > 0.5$			$\lvert\gamma_{c_p}\rvert > 0.5$ or $\lvert\kappa_{c_p}\rvert > 0.5$		
	0°	45°	90°	0°	45°	90°	0°	45°	90°
SLF	21.2	23.5	22.4	24.7	45.9	58.8	27.1	47.1	60.0
SHF	31.5	21.3	36.0	46.1	42.7	57.3	47.2	43.8	57.3
SLC	11.2	21.3	34.8	21.3	29.2	67.4	21.3	32.6	68.5
SHC	10.1	7.9	42.7	23.6	23.6	71.9	24.7	23.6	73.0
RLF	18.9	27.4	33.7	24.2	41.1	67.4	27.4	49.5	73.7
RHF	31.6	15.8	52.6	32.6	31.6	72.6	35.8	37.9	78.9
RLC	14.7	30.5	48.4	20.0	40.0	81.1	24.2	46.3	88.4
RHC	16.8	16.8	17.9	22.1	20.0	43.2	24.2	26.3	51.6
Average	19.5	20.6	36.1	26.8	34.3	65.0	29.0	38.4	68.9

all values are in %

The percentage on non-Gaussian pressure coefficient processes is highest for θ = 90° for all physical models, whereas this percentage is higher for θ = 45° than for θ = 0° in all cases with the exception of models SHF and SHC. For all models, the percentage of non-Gaussian pressure coefficient processes for θ = 90° is higher than 50%, with the maximum value equal to 88.4% for model RLC and the minimum value equal to 51.6% for RHC. For θ = 0° and 45°, this percentage is lower than 50% for all models. The same increasing trend is observed for the percentages of pressure taps where the skewness or excess kurtosis coefficient is larger than 0.5 in absolute value.

The shape of the physical models seems to have a significant influence on the percentage of non-Gaussian pressure coefficient processes, albeit smaller than that of the wind angle of attack. In particular, for θ = 90°, the percentage of non-Gaussian pressure coefficient processes is generally higher for rectangular models than for the corresponding square models, with the exception of model RHC, for which the lowest percentage of non-Gaussian pressure coefficient process is observed (i.e., 51.6%). However, this observation does not hold for θ = 0° and 45°, for which the same percentages are generally similar between corresponding square and rectangular models. Higher curvature roof models have lower percentages of non-Gaussian pressure coefficient processes for θ = 0° and 45°, but

higher percentages for θ = 90°, with the exception of model RHC that has lower percentages than model RHF also for θ = 90°. No clear trend can be recognized between corresponding models of different height.

5. EXPERIMENTAL PEAK FACTORS

The second phase of this investigation focuses on the experimental PFs of the pressure coefficients measured at different locations for different roof geometries through wind tunnel tests (Rizzo et al. 2011).

The experimental PFs for the entire time history, g_{T_0}, were obtained as:

$$g_{T_0} = \frac{\max_{0 \le t \le T_0} \left[c_p(t) \right] - \mu_{c_p}}{\sigma_{c_p}} \tag{1}$$

where t denotes time, and $c_p(t)$ represents the recorded time history of the wind pressure coefficient.

Table 9 reports the experimental minimum and maximum values of the PFs for different models and wind attack angles in different zones of the considered roofs. It is observed that the maximum values of the PFs reach values higher than 10 for several models and wind angles values, particularly in zones B and C, clearly indicating a strongly non-Gaussian behavior. The minimum values of the PFs in the different regions assume values generally contained between 3 and 4, with a few cases that are as high as 5, indicating that pressure taps that are located within the same regions (and thus relatively close to each other) may experience approximately Gaussian and strongly non-Gaussian behaviors for any given angle and model.

In contrast with the quantities reported in the previous sections of this paper, which represents the statistics of the random pressure coefficients, the PFs measured over the entire records (T_0 = 29.77 s) can be interpreted as single realizations of the random PFs $\left(g_{T_0} \right)$ and, thus, are expected to change (sometimes even drastically) from experiment to

experiment.

Table 9. Experimental minimum and maximum PFs for different models and attack angles.

Zone	Model	Max/Min	Square			Rectangular		
			0°	45°	90°	0°	45°	90°
A	SLF/RLF	Max	5.847	6.490	8.637	5.409	5.766	7.512
		Min	4.086	4.075	3.657	3.720	4.003	4.452
	SHF/RHF	Max	5.970	7.244	8.365	4.895	4.826	8.707
		Min	3.932	3.053	4.377	2.813	3.126	4.021
	SLC/RLC	Max	5.481	5.022	8.483	6.080	7.981	7.352
		Min	3.457	3.939	2.334	3.749	3.629	4.152
	SHC/RHC	Max	5.347	5.253	9.547	5.684	6.928	7.401
		Min	3.234	3.487	4.093	3.484	3.534	3.725
B	SLF/RLF	Max	10.405	7.366	9.216	6.073	7.440	10.360
		Min	2.985	4.263	3.806	3.905	4.156	4.393
	SHF/RHF	Max	11.410	5.483	9.357	14.152	7.201	11.531
		Min	3.953	3.531	5.102	3.760	3.381	5.173
	SLC/RLC	Max	8.539	5.633	13.902	8.303	7.149	9.494
		Min	3.888	3.491	5.140	3.513	3.526	4.753
	SHC/RHC	Max	10.338	5.684	11.339	8.719	6.928	7.401
		Min	4.340	3.519	4.858	3.640	3.314	4.163
C	SLF/RLF	Max	10.478	11.201	5.949	6.940	6.958	9.909
		Min	3.786	4.263	3.564	3.355	3.688	4.057
	SHF/RHF	Max	12.115	8.116	6.270	14.816	5.976	8.158
		Min	4.223	4.277	3.606	3.711	3.381	4.866
	SLC/RLC	Max	6.047	8.077	8.540	7.609	9.907	6.882
		Min	3.864	3.896	3.506	3.523	3.526	4.040
	SHC/RHC	Max	10.294	13.531	10.115	9.132	7.367	6.021
		Min	3.785	3.385	3.900	3.724	3.732	3.725
D	SLF/RLF	Max	5.768	7.999	7.656	6.219	7.535	6.598
		Min	3.323	3.592	4.175	3.355	4.597	3.837
	SHF/RHF	Max	7.134	7.785	9.388	4.290	8.249	4.894
		Min	3.960	3.713	3.945	3.318	3.971	3.709
	SLC/RLC	Max	6.146	6.687	10.642	6.554	7.300	6.399
		Min	3.468	3.747	3.678	3.425	4.349	4.137
	SHC/RHC	Max	5.450	6.681	8.658	7.023	6.393	5.062
		Min	3.792	3.776	3.948	3.792	3.990	3.740
E	SLF/RLF	Max	6.567	7.999	6.326	6.073	15.897	6.284
		Min	2.985	3.315	3.835	3.133	3.330	3.605
	SHF/RHF	Max	6.966	10.801	6.117	8.188	7.824	7.044
		Min	3.256	3.180	3.437	3.189	2.890	3.678
	SLC/RLC	Max	6.067	7.300	6.268	4.959	8.418	7.689
		Min	3.064	3.345	3.537	2.993	3.133	3.722
	SHC/RHC	Max	5.888	5.824	7.316	7.023	7.812	8.335
		Min	3.067	2.956	3.562	3.328	3.208	3.415

In order to investigate the statistics of the PFs (i.e., means and standard deviations), the experimental records were divided into shorter intervals of T_1 = 0.99 s, for each of which a sample realization of the PFs was calculated as

$$g_{T_1}^{(j)} = \frac{\max\limits_{(j-1)\cdot T_1 \le t \le j\cdot T_1} \left[c_p(t) \right] - \mu_{c_p}}{\sigma_{c_p}}; \quad j = 1,2,\ldots,30 \tag{2}$$

Using the 30 sample realizations of the PFs for each of these smaller intervals $(g_{T_1}^{(j)}, j = 1,2,\ldots,30)$, the corresponding sample means ($\mu_{g_{T_1}}$) and sample standard deviations $\left(\sigma_{g_{T_1}}\right)$ were calculated and are reported in Figure 6 through Figure 11 for all geometries, attack angles, and pressure taps. The time duration of the sub-intervals was purposely selected to obtain a sufficient number of samples and achieve a stable (i.e., approximately converged) estimate of the peak factor's means and standard deviations. It is also observed that the sample peak factors for the entire time history and for the shorter intervals do not have the same physical meaning of the so-called peak factors used in modern design codes and standards (e.g., ASCE 2016, CEN 2005), which effectively correspond to the mean values of the peak factors calculated for a conventional time duration, usually taken as 1 hour or 10 minutes. The experimental peak factors obtained in this study are used to assess the accuracy of the peak factor's means and standard deviations estimated using different analytical models. This assessment can be performed with reference to any arbitrary time duration, *T*, without loss of generality. In fact, once an appropriate analytical model is established, the analytical peak factor's means and standard deviations can be scaled to correspond to the desired time duration for use in design, as they depend on *T* through the quantity $\ln(\nu_0 \cdot T)$ (see Appendix A). Finally, it is highlighted that the use of μ_{c_p} and σ_{c_p} in Eq. (2) (i.e., the pressure coefficient mean and standard deviation estimated using the entire time history) is justified by the assumptions of stationarity and ergodicity of the underlying

stochastic processes.

5.1 Peak factor statistics for θ = 0°

For θ = 0° (Figures 6 and 7), a strong correlation between large values of the PF means and standard deviations is observed. In fact, for both square and rectangular shapes, the largest values of PF means and standard deviations are achieved in zones B and C, as well as in portions of zone E that are close to B and C.

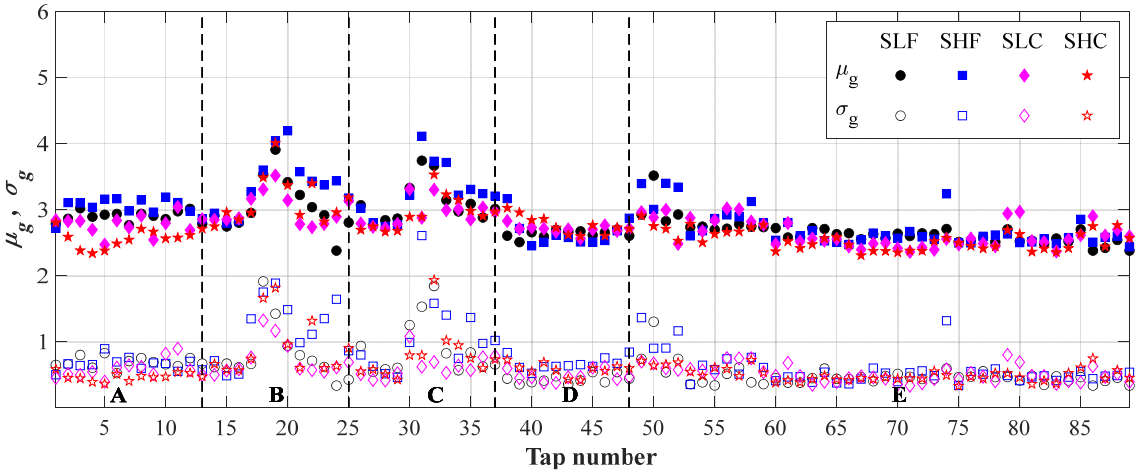

Figure 6. Sample means and standard deviation of PFs for T_1 = 0.99 s, square plans, and θ = 0°.

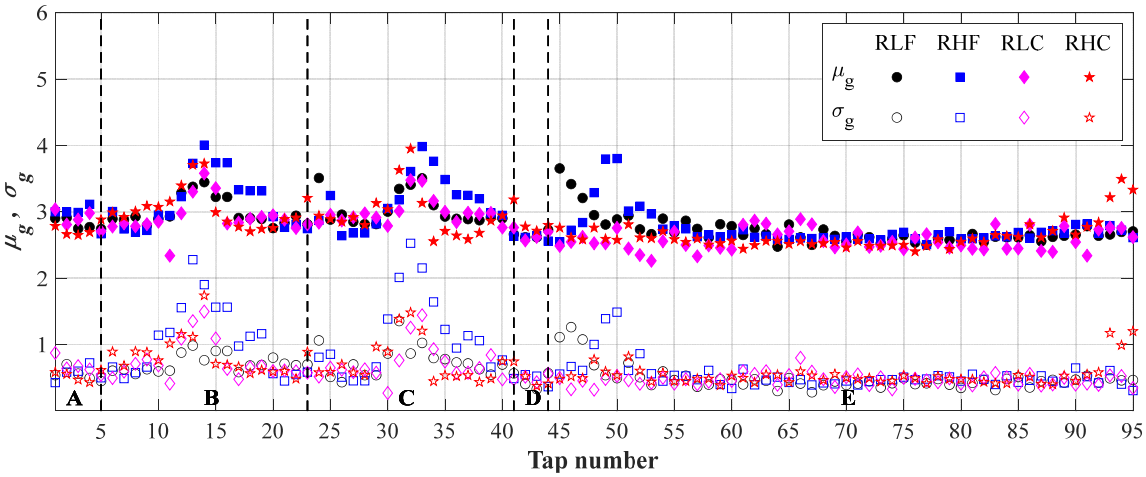

Figure 7. Sample means and standard deviation of PFs for T_1 = 0.99 s, rectangular plans, and θ = 0°.

The dependence of the PF statistics on the model geometry is relatively small when compared to the dependence on the pressure tap location, with models SHF and RHF

showing generally higher PF means and standard deviations than all other models. The variability of the PF standard deviations is systematically higher than the variability of the PF mean, both among different models and within the same models in different zones.

5.2 Peak factor statistics for θ = 45°

For θ = 45° (Figures 8 and 9), the variability of the PF means and standard deviations is smaller than for θ = 0°. In this case, it is not possible to identify specific model geometries or roof zones with higher values of the PF means and standard deviations, as it was done in the previous case.

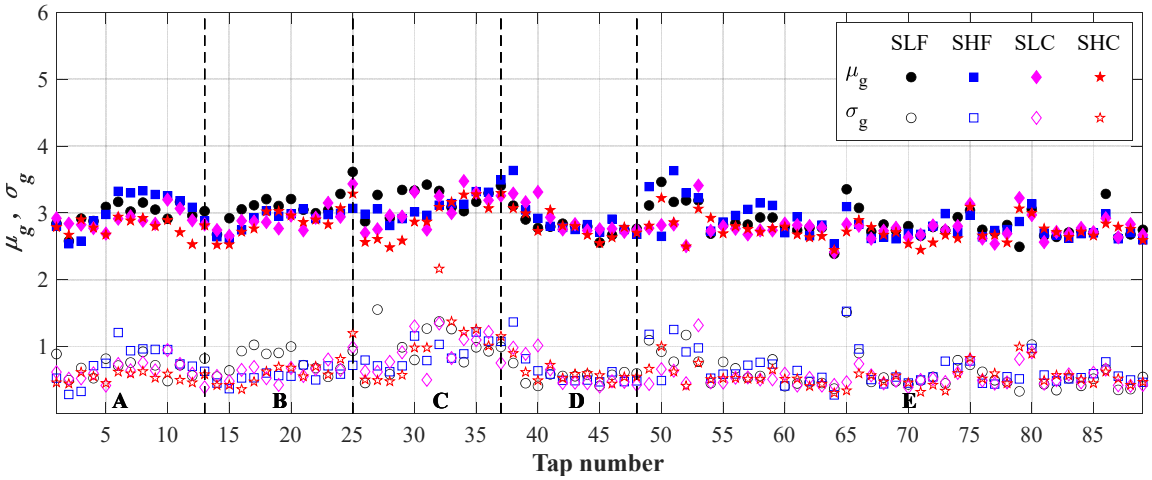

Figure 8. Sample means and standard deviation of PFs for T_1 = 0.99 s, square plans, and θ = 45°.

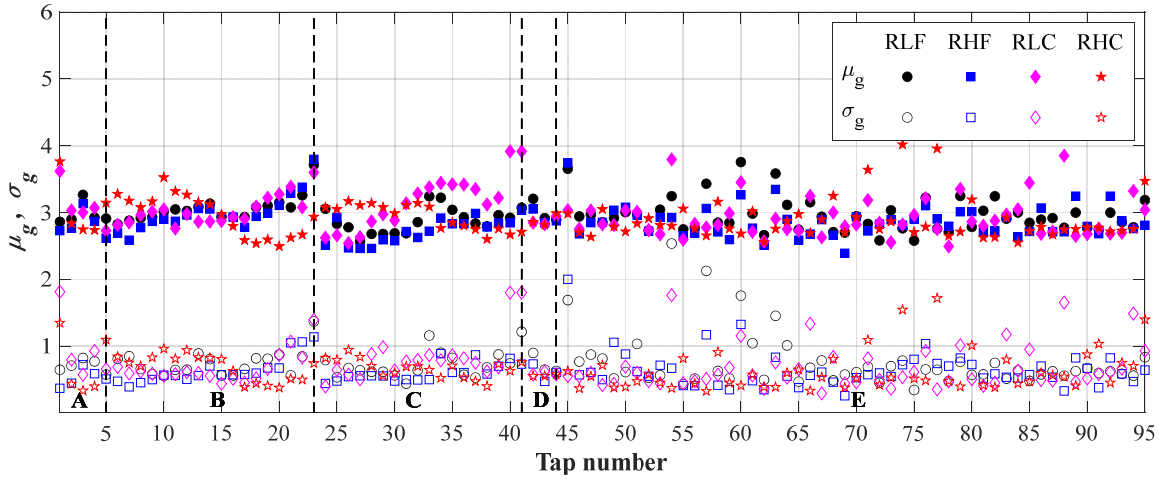

Figure 9. Sample means and standard deviation of PFs for T_1 = 0.99 s, rectangular plans, and θ =

45°.

The PF statistics assume generally lower values in the square plans than in the rectangular ones and are generally lower than for the corresponding model geometry and roof zone with θ = 0°.

5.3 Peak factor statistics for θ = 90°

For θ = 90° (Figures 10 and 11), an even smaller variability in the PF means is observed than for θ = 45°, particularly for the model geometries with rectangular plans.

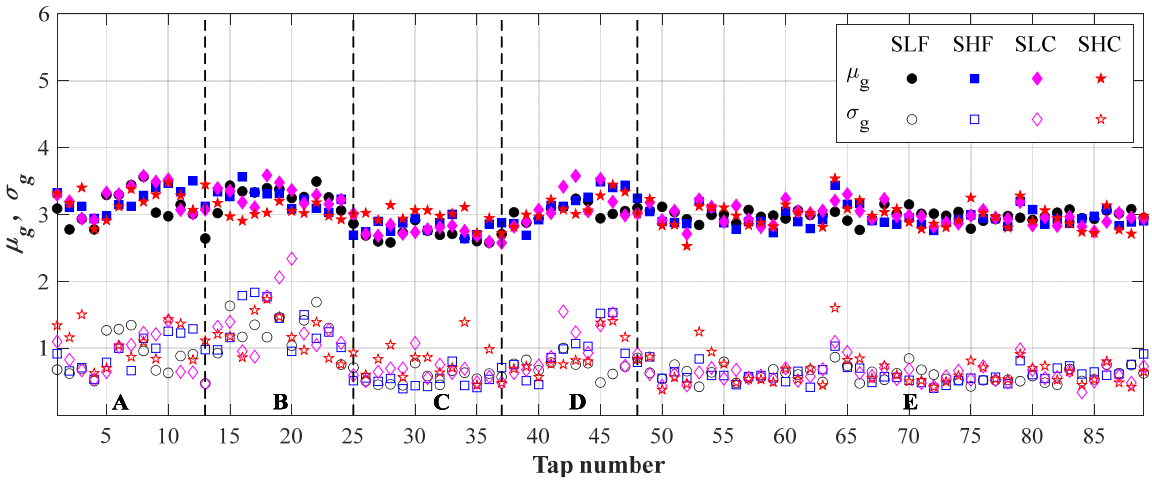

Figure 10. Sample means and standard deviation of PFs for T_1 = 0.99 s, square plans, and θ = 90°.

In all cases, the PF means are significantly lower than 4 at all locations. Higher values of the PF standard deviations do not necessarily correspond to higher values of the PF means. For both square and rectangular plans, the PF standard deviations are lower than 2, with the exception of 2 pressure taps for model SLC, 2 pressure taps for model RHF, and 1 pressure tap for model RLF, all located in roof zone B.

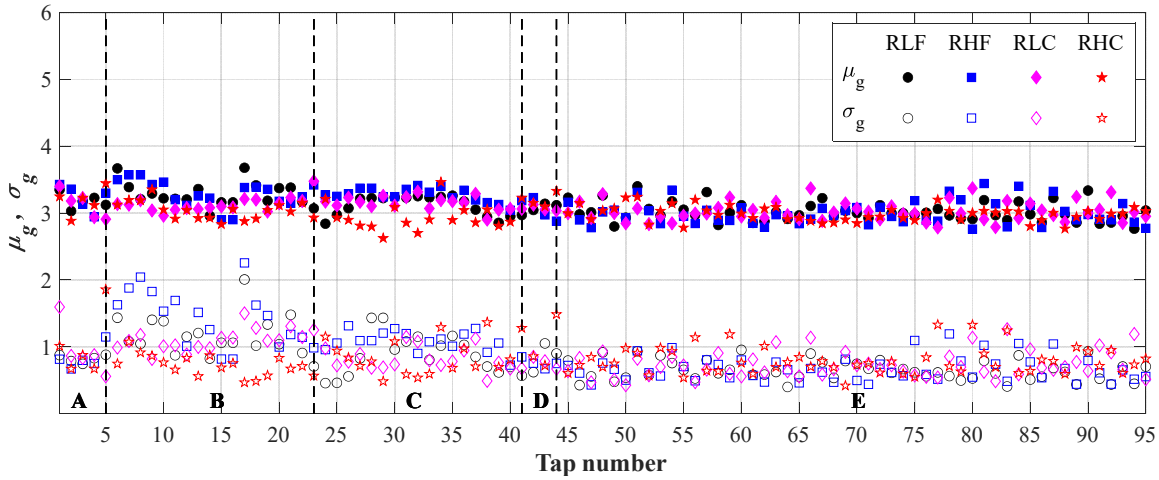

Figure 11. Sample means and standard deviation of PFs for T_1 = 0.99 s, rectangular plans, and θ = 90°.

6. COMPARISON OF EXPERIMENTAL PEAK FACTOR STATISTICS WITH ANALYTICAL MODELS

The experimental PF statistics calculated using sub-intervals T_1 = 0.99 s of the acquired time-histories (i.e., mean $\mu_{g_{T_1}}$ and standard deviation $\sigma_{g_{T_1}}$) are compared here with the corresponding estimates obtained using the following three analytical models that are widely adopted in the literature (see Appendix A): the Davenport (D) model (Davenport, 1964), the modified Hermite (mH) model (Kwon and Kareem 2011), and the Translated-Peak-Process (TTP) model (Huang et al. 2013). In order to assess the global accuracy of the considered analytical models under different wind angles–(i.e., θ = 0°, 45°, and 90°) and different geometries (i.e. square and rectangular plan, low and high models, and flatter and more curved roof), the modified root mean square error (mRMSE) proposed by Peng et al. (2014) and used in Rizzo et al. (2018) is also adopted in this study. The mRMSE for the PF means, $\varepsilon_{\mathrm{M},T_1}$, and standard deviations, δ_{M,T_1} are defined as:

$$\varepsilon_{\mathrm{M},T_1} = \sqrt{\frac{1}{n}\sum_{i=1}^{n} S_i^2} \tag{3}$$

$$\delta_{\mathrm{M},T_1} = \sqrt{\frac{1}{n}\sum_{i=1}^{n} Z_i^2} \tag{4}$$

respectively, in which

$$S_i = \begin{cases} \mu_{\mathrm{M},g_{T_1}}^{(i)} - \mu_{\exp,g_{T_1}}^{(i)} - 2SE_{\mu}^{(i)} & \text{if} \quad \mu_{\mathrm{M},g_{T_1}}^{(i)} - \mu_{\exp,g_{T_1}}^{(i)} > 2SE_{\mu}^{(i)} \\ 0 & \text{if} \quad \left|\mu_{\mathrm{M},g_{T_1}}^{(i)} - \mu_{\exp,g_{T_1}}^{(i)}\right| \le 2SE_{\mu}^{(i)} \\ \mu_{\mathrm{M},g_{T_1}}^{(i)} - \mu_{\exp,g_{T_1}}^{(i)} + 2SE_{\mu}^{(i)} & \text{if} \quad \mu_{\mathrm{M},g_{T_1}}^{(i)} - \mu_{\exp,g_{T_1}}^{(i)} < -2SE_{\mu}^{(i)} \end{cases} \tag{5}$$

$$Z_i = \begin{cases} \sigma_{\mathrm{M},g_{T_1}}^{(i)} - \sigma_{\exp,g_{T_1}}^{(i)} - 2SE_{\sigma}^{(i)} & \text{if} \quad \sigma_{\mathrm{M},g_{T_1}}^{(i)} - \sigma_{\exp,g_{T_1}}^{(i)} > 2SE_{\sigma}^{(i)} \\ 0 & \text{if} \quad \left|\sigma_{\mathrm{M},g_{T_1}}^{(i)} - \sigma_{\exp,g_{T_1}}^{(i)}\right| \le 2SE_{\sigma}^{(i)} \\ \sigma_{\mathrm{M},g_{T_1}}^{(i)} - \sigma_{\exp,g_{T_1}}^{(i)} + 2SE_{\sigma}^{(i)} & \text{if} \quad \sigma_{\mathrm{M},g_{T_1}}^{(i)} - \sigma_{\exp,g_{T_1}}^{(i)} < -2SE_{\sigma}^{(i)} \end{cases} \tag{6}$$

in which the index i indicates the number of the pressure tap; $\mu_{\exp,g_{T_1}}^{(i)}$ and $\sigma_{\exp,g_{T_1}}^{(i)}$ denote the experimental PF mean and standard deviation at pressure tap *i*, respectively; $n = 89$ for square plans and $n = 95$ for rectangular plans denotes the total number of pressure taps on the roof models; $SE_{\mu}^{(i)}$ and $SE_{\sigma}^{(i)}$ denote the standard error for the experimental estimate of the PF mean and standard deviation at pressure tap *i*, respectively; and M = D, mH, or TPP denotes the analytical model used to estimate the PF mean $\mu_{\mathrm{M},g_{T_1}}^{(i)}$ and standard deviation $\sigma_{\mathrm{M},g_{T_1}}^{(i)}$ at pressure tap *i*.

Table 10 and Table 11 report the mRMSE for the PF mean estimates of different analytical models corresponding to model geometries with square and rectangular plans, respectively. It is observed that the mH model provides the best approximations for the PF means over the entire roof geometries, with the exception of one case for the square plans (i.e., SLC model with θ = 90°) and two cases for the rectangular plans (i.e., RLF model with θ = 45° and RHF model with θ = 0°), for which the TPP model provides the best estimates of the PF means.

Table 10. mRSME for the PF mean estimates of different analytical models applied to different model geometries with square plans and different attack angles (bold text used for smallest mRSME).

Geometry	θ	D	mH	TPP
SLF	0°	0.243	**0.087**	0.092
	45°	0.275	**0.123**	0.153
	90°	0.311	**0.056**	0.097
SHF	0°	0.343	**0.108**	0.123
	45°	0.269	**0.164**	0.188
	90°	0.335	**0.072**	0.096
SLC	0°	0.200	**0.059**	0.082
	45°	0.234	**0.074**	0.117
	90°	0.347	0.300	**0.154**
SHC	0°	0.206	**0.183**	0.191
	45°	0.177	**0.134**	0.143
	90°	0.315	**0.165**	0.169

Table 11. mRSME for the PF mean estimates of different analytical models applied to different model geometries with rectangular plans and different attack angles (bold text used for smallest mRSME).

Geometry	θ	D	mH	TPP
RLF	0°	0.264	**0.081**	0.108
	45°	0.272	0.196	**0.191**
	90°	0.359	**0.114**	0.161
RHF	0°	0.307	0.104	**0.077**
	45°	0.216	**0.103**	0.119
	90°	0.365	**0.116**	0.145
RLC	0°	0.193	**0.112**	0.132
	45°	0.305	**0.077**	0.098
	90°	0.339	**0.157**	0.188
RHC	0°	0.255	**0.097**	0.114
	45°	0.296	**0.061**	0.091
	90°	0.311	**0.099**	0.132

This conclusion confirms the results reported in Rizzo et al. (2018) for a single geometry of HPRs. In general, the mRSME are close for the mH and the TPP models, whereas the errors corresponding to the D model are significantly larger, generally between 2 and 4 times the errors of the other two models. This result indicates that both the mH and the TPP model are able to capture the non-Gaussianity of the processes describing the PFs on HPRs.

Table 12 and Table 13 report the mRMSE for the PF standard deviation estimates of different analytical models corresponding to model geometries with square and rectangular plans, respectively. For the PF standard deviation, it is observed that the TPP model provides the best approximations over the entire roof geometries, with the exception of one case for

the square plans (i.e., SHF model with θ = 45°) and two cases for the rectangular plans (i.e., RLF model with θ = 45° and RHF model with θ = 0°), for which the mH model provides the best estimates of the PF standard deviation. Also this conclusion confirms the results reported in Rizzo et al. (2018) for a single geometry of HPRs. In general, also for this quantity, the mRSME are close for the mH and the TPP models, whereas the errors corresponding to the D model are significantly larger, generally about twice the errors of the other two models. Also this result indicates that both the mH and the TPP model are able to capture the non-Gaussianity of the processes describing the PFs on HPRs.

Table 12. mRSME for the PF standard deviation estimates of different analytical models applied to different model geometries with square plans and different attack angles (bold text used for smallest mRSME).

Geometry	θ	D	mH	TPP
SLF	0°	0.172	0.098	**0.075**
	45°	0.140	0.119	**0.071**
	90°	0.165	0.091	**0.029**
SHF	0°	0.254	0.095	**0.078**
	45°	0.132	0.098	**0.083**
	90°	0.205	0.122	**0.049**
SLC	0°	0.092	0.116	**0.085**
	45°	0.103	0.105	**0.066**
	90°	0.236	0.112	**0.067**
SHC	0°	0.170	0.063	**0.048**
	45°	0.149	**0.090**	0.097
	90°	0.212	0.099	**0.056**

Table 13. mRSME for the PF standard deviation estimates of different analytical models applied to different model geometries with rectangular plans and different attack angles (bold text used for smallest mRSME).

Geometry	θ	D	mH	TPP
RLF	0°	0.101	0.093	**0.061**
	45°	0.217	**0.102**	0.123
	90°	0.189	0.088	**0.055**
RHF	0°	0.310	**0.115**	0.120
	45°	0.132	0.106	**0.067**
	90°	0.281	0.080	**0.058**
RLC	0°	0.130	0.083	**0.065**
	45°	0.166	0.118	**0.064**
	90°	0.158	0.068	**0.018**
RHC	0°	0.138	0.080	**0.043**
	45°	0.139	0.109	**0.064**
	90°	0.144	0.090	**0.040**

7. CONCLUSIONS

The statistics of pressure coefficient records acquired with wind tunnel tests on eight different geometries of hyperbolic paraboloid roofs are investigated to identify the conditions under which non-Gaussian behavior is prevalent. The considered geometries consisted of square and rectangular plan shapes with two heights (i.e., high and low) and two roof curvatures (i.e., flatter and more curved). Three significant wind angles of attack are considered (i.e., 0°, 45°, and 90°). The distribution on the roof of the considered pressure coefficient statistics is investigated by subdividing the roof into five zones (i.e., A, B, C, D and E), selected in order to study where Gaussian and non-Gaussian processes are located. The location on the roof and the wind angle of attack are the most important parameters affecting the statistics of the pressure coefficients, followed by the plan shape, the height of the building, and finally the roof curvature. In general, the pressure coefficients are (sometimes strongly) non-Gaussian along the edges of the models, whereas they are approximately Gaussian in portions of the zones at the center of the roofs.

PFs extracted from these pressure coefficient time histories are also compared with estimated values calculated by using three analytical models available in the literature, i.e., the Davenport, modified Hermite, and Translated Peak Process (TPP) models. The obtained results are presented and discussed both for entire time histories and for smaller interval series in order to compare PF means and standard deviations. Results show that, in general, the modified Hermite model provides the best overall estimates of the PF means, whereas the TPP model provides the best overall estimates of the PF standard deviations.

The Davenport model is able to provide reasonable approximations of the PF means and standard deviations only in zones located in the middle of the roofs, where the pressure coefficients are approximately Gaussian. This study also confirms that the conventional PF of 3.5 (typically used under the assumption of Gaussianity for the pressure coefficient

processes) is not representative of the PFs for hyperbolic paraboloid roofs with the geometries considered in this study. Finally, it is noteworthy that the results of this study largely confirm, over multiple HPR shapes and geometries, the results presented in Rizzo et al. (2018) for a single HPR geometry, thus suggesting that the conclusions from this study may be generally applicable to HPR structures.

Further investigations are needed to implement the results of the present study into design guidelines aimed to avoid local instability phenomena in flexible HPRs, such as loss of tension and curvature inversion in cables, which can be controlled by unfavorable combinations of wind pressure maxima and minima.

DATA AVAILABILITY STATEMENT

All data, models, and code generated or used during the study appear in the submitted article.

ACKNOWELDGEMENTS

The second author gratefully acknowledges partial support for this research by the University of California Office of the President (UCOP) Lab Fees Program through award LFR-20-651032. Any opinions, findings, conclusions, or recommendations expressed in this publication are those of the authors and do not necessarily reflect the views of the sponsoring agency.

APPENDIX A: Analytical Estimates of Peak Factor's Mean and Standard Deviation

The analytical estimates of the peak factor's mean and standard deviation for the Davenport model (Davenport, 1964) and duration *T* are given by:

$$\mu_{g,\mathrm{D}}(T) = \beta(T) + \frac{\gamma}{\beta(T)} \tag{7}$$

$$\sigma_{g,\mathrm{D}}(T) = \frac{\pi}{\beta(T)\cdot\sqrt{6}} \tag{8}$$

where $\gamma \approx 0.5772$ and $\beta(T) = \sqrt{2 \cdot \ln(\nu_0 \cdot T)}$.

The analytical estimates of the peak factor's mean and standard deviation for the modified Hermite (mH) model (Kwon and Kareem 2011) and duration *T* are given by:

$$\mu_{g,\mathrm{mH}}(T) = k \cdot \left[\mu_{g,\mathrm{D}}(T) + h_3 \cdot f_1(T) + h_4 \cdot f_2(T) \right] \tag{9}$$

$$\sigma_{g,\mathrm{mH}}(T) = k \cdot \sqrt{\sigma^2_{g,\mathrm{D}}(T) + 6.58 h_3^2 \cdot f_3(T) + 9 h_4^2 \cdot f_4(T) + 6 h_4 \cdot f_5(T) + 12 h_3 h_4 \cdot f_6(T)} \tag{10}$$

where:

$$f_1(T) = \beta^2(T) + 2\gamma - 1 + \frac{1.98}{\beta^2(T)} \tag{11}$$

$$f_2(T) = \beta^3(T) + 3\beta(T) \cdot (\gamma - 1) + \frac{3}{\beta(T)} \cdot \left(\frac{\pi^2}{6} - \gamma + \gamma^2 \right) + \frac{5.44}{\beta^3(T)} \tag{12}$$

$$f_3(T) = 1 + \frac{1}{h_3 \cdot \beta(T)} \tag{13}$$

$$f_4(T) = 1.64\beta^2(T) + \frac{12.69}{\beta^2(T)} + 5.32 \tag{14}$$

$$f_5(T) = \frac{2.66}{\beta^2(T)} + 1.64 \tag{15}$$

$$f_6(T) = 1.64\beta(T) + \frac{2.66}{\beta(T)} \tag{16}$$

$$h_3 = \begin{cases} \dfrac{\gamma_{c_p}}{4 + 2\sqrt{1 + 1.5\kappa_{c_p}}} & \text{if} \quad -\gamma_{c_p} + \left(1.25\kappa_{c_p}\right)^2 > 0 \\ f_7\left(\gamma_{c_p}, \kappa_{c_p}\right) & \text{if} \quad -\gamma_{c_p} + \left(1.25\kappa_{c_p}\right)^2 \le 0 \end{cases} \tag{17}$$

$$h_4 = \begin{cases} \dfrac{\sqrt{1 + 1.5\kappa_{c_p}} - 1}{18} & \text{if} \quad -\gamma_{c_p} + \left(1.25\kappa_{c_p}\right)^2 > 0 \\ f_8\left(\gamma_{c_p}, \kappa_{c_p}\right) & \text{if} \quad -\gamma_{c_p} + \left(1.25\kappa_{c_p}\right)^2 \le 0 \end{cases} \tag{18}$$

$$k = \frac{1}{\sqrt{1 + 2h_3^2 + 6h_4^2}} \tag{19}$$

and $f_7\left(\gamma_{c_p},\kappa_{c_p}\right)$ and $f_8\left(\gamma_{c_p},\kappa_{c_p}\right)$ are polynomial functions given in Yang et al. (2013)

The analytical estimates of the peak factor's mean and standard deviation for the TTP model (Huang et al. 2013) and duration *T* are given by:

$$\mu_{g,\mathrm{TTP}}(T)=\left[\rho\cdot\ln\left(\nu_0\cdot T\right)\right]^{\frac{1}{\kappa}}+\frac{\gamma\cdot\left[\rho\cdot\ln\left(\nu_0\cdot T\right)\right]^{\frac{1}{\kappa}}}{\kappa\cdot\ln\left(\nu_0\cdot T\right)} \tag{20}$$

$$\sigma_{g,\mathrm{TTP}}(T)=\frac{\pi}{\sqrt{6}}\cdot\frac{\left[\rho\cdot\ln\left(\nu_0\cdot T\right)\right]^{\frac{1}{\kappa}}}{\kappa\cdot\ln\left(\nu_0\cdot T\right)} \tag{21}$$

where κ = shape parameter and ρ = scale parameter of the peak distribution corresponding to a Weibull peak model obtained from a point-to-point mapping of the peak data.

REFERENCES

[1] Alrawashdeh H., Stathopoulos T., 2015. Wind pressures on large roofs of low buildings and wind codes and standards. *Journal of Wind Engineering and Industrial Aerodynamics*, 147, 212-225.

[2] American Society of Civil Engineers (ASCE). 2016. *Minimum Design Loads and Associated Criteria for Buildings and Other Structures.* ASCE/SEI 7-16. Reston, VA (USA).

[3] Barbato M., Petrini F., Unnikrishnan V.U., Ciampoli M., 2013. Performance-based hurricane engineering (PBHE) framework. *Structural Safety*, 45, 24–35.

[4] National Research Council of Italy (CNR), 2018. *Guide for the Assessment of Wind Actions and Effects on Structures*. CNR-DT 207/2018, Rome (Italy).

[5] European Committee for Standardization (CEN), 2005. *Eurocode 1: Actions on Structures - Part 1-4: General Actions - Wind Actions*. EN-1991-1-4, Brussels (Belgium).

[6] Chilton J., 2010. *Tensile Structures-Textiles for Architecture and Design*. In: Pöhl G. ed. Textile Polymers and Composites for Buildings. Woodhead Publishing Limited, Cambridge, England (UK), 229–257.

[7] Ciampoli M., Petrini F., 2012. Performance-based Aeolian risk assessment and reduction for tall buildings. *Probabilistic Engineering Mechanics*, 28, 75–84.

[8] Colliers J., Mollaert M., Degroote J., De Laet L., 2019. Prototyping of thin shell wind tunnel models to facilitate experimental wind load analysis on curved canopy structures. *Journal of Wind Engineering and Industrial Aerodynamics*, 188, 308-322

[9] Colliers J., Degroote J., Mollaert M., De Laet L., 2020. Mean pressure coefficient distributions over

hyperbolic paraboloid roof and canopy structures with different shape parameters in a uniform flow with very small turbulence. *Engineering Structures*, 205, 110043

[10] Colliers J., Mollaert M., Vierendeels J., De Laet L., 2016. Collating wind data for doubly-curved shapes of tensioned surface structures (Round Robin Exercise 3). *Procedia Engineering*, 155, 152-162.

[11] Davenport A.G., 1964. Note on the distribution of the largest value of a random function with application to gust loading. *Institution of Civil Engineering*, 28(2), 187–196.

[12] Elashkar I., Novak M., 1983, Wind tunnel studies of cable roofs. *Journal of Wind Engineering and Industrial Aerodynamics*, 13, 1–3, 407–419.

[13] Foster B., Mollaert M., 2004. *The European Design Guide for Tensile Surface Structures*. TensiNet, Brussels (Belgium).

[14] Gurley K.R., Tognarelli M.A., Kareem A., 1997. Analysis and simulation tools for wind engineering. *Probabilistic Engineering Mechanics*, 12(1), 9–31.

[15] Huang M.F., Lou W., Chan C.M., Lin N., Pan X., 2013. Peak distributions and peak factors of wind-induced pressure processes on tall buildings. *Journal of Engineering Mechanics*, 139(12), 1744-1756.

[16] Huntington C.G., 2004. *The Tensioned Fabric Roof*. American Society of Civil Engineers (ASCE), Reston, VA (USA).

[17] Huntington C.G., 2013. *Tensile Fabric Structures. Design, Analysis, and Construction.* American Society of Civil Engineers (ASCE), Reston, VA (USA).

[18] Kareem A., Zhao J., 1994. Analysis of non-Gaussian surge response of tension leg platforms under wind loads. *Journal of Offshore Mechanics and Arctic Engineering*, 116(3), 137-144.

[19] Kwon D., Kareem A., 2011. Peak factors for non-Gaussian load effects revisited. *Journal of Structural Engineering*, 137(12), 1611-1619.

[20] Letchford C.W., Denoon R.O., Johnson G., Mallam A., 2002. Dynamic characteristics of cantilever grandstand roofs. *Engineering Structures*, 24(8), 1085-1090.

[21] Liu M., Chen X., Yang Q., 2016. Characteristics of dynamic pressures on a saddle type roof in various boundary layer flows. *Journal of Wind Engineering and Industrial Aerodynamics*, 150, 1–14.

[22] Liu M., Chen X., Yang Q., 2017. Estimation of peak factor of non-Gaussian wind pressures by improved moment-based Hermite model. *Journal of Engineering Mechanics*, 143(7):06017006.

[23] Majowiecki M., 2004. *Tensostrutture: Progetto e Controllo*. Edizioni Crea, Milan (Italy), in italian.

[24] Peng X., Yang L., Gavanski E., Gurley K., Prevatt D., 2014. A comparison of methods to estimate peak

wind loads on buildings. *Journal of Wind Engineering and Industrial Aerodynamics*, 126, 11–23.

[25] Rizzo F., D'Asdia P., Lazzari M., Procino L., 2011. Wind action evaluation on tension roofs of hyperbolic paraboloid shape. *Engineering Structures*, 33(2), 445–461.

[26] Rizzo F., 2014. *Aerodynamics of Tensile Structures.* Silvana Editoriale, Cinisello Balsamo, Milano (Italy), ISBN-10: 8836628400.

[27] Rizzo F., Zazzini P., 2016. Improving the acoustical properties of an elliptical plan space with a cable net membrane roof. *Acoustics Australia*, 44, 449-456, (11-16-2016) ISSN: 08146039.

[28] Rizzo F., Zazzini P., 2017. Shape dependence of acoustic performances in buildings with a Hyperbolic Paraboloid cable net membrane roof. *Acoustics Australia*, 45 (2), (01-01-2017) 421–443, ISSN: 08146039, DOI: 10.1007/s40857-017-0092-9.

[29] Rizzo F., Ricciardelli F., 2017. Design pressure coefficients for circular and elliptical plan structures with hyperbolic paraboloid roof. *Engineering Structures*, 139, 153-169.

[30] Rizzo F., Barbato M., Sepe V., 2018. Peak factor statistics of wind effects for hyperbolic paraboloid roofs. *Engineering Structures*, 173, 313-330.

[31] Rizzo F., Sepe V., Ricciardelli F., Avossa A.M., 2020. Wind pressures on a large span canopy roof. *Wind and Structures*, 30(3), 299-316.

[32] Sadek F., Simiu E., 2002. Peak non-Gaussian wind effects for database-assisted low-rise building design. *Journal of Engineering Mechanics*, 128(5), 530-539.

[33] Suresh Kumar K., Stathopoulos T., 2000. Wind loads on low building roofs: a stochastic perspective. *Journal of Structural Engineering*, 126(8), 944-956.

[34] Unnikrishnan V.U., Barbato M., 2016. Performance-based comparison of different storm mitigation techniques for residential buildings. *Journal of Structural Engineering*, 142(6):04016011.

[35] . Vassilopoulou I., Gantes C.J., 2012. Vibration modes and natural frequencies of saddle form cable nets. *Computers and Structures*, 88(1-2), 105-119.

[36] Vassilopoulou, I., Petrini, F., Gantes, C.J., 2017. Nonlinear Dynamic Behavior of Cable Nets Subjected to Wind Loading, Structures, 10, 170-183.

[37] Yang L., Gurley K.R., Prevatt D.O., 2013. Probabilistic modeling of wind pressure on low-rise buildings. *Journal of Wind Engineering & Industrial Aerodynamics*, 114, 18–26.